



CHORUS

This is the accepted manuscript made available via CHORUS. The article has been published as:

Manipulation of Electronic Transport in the Bi(111) Surface State

G. Jnawali, C. Klein, Th. Wagner, H. Hattab, P. Zahl, D. P. Acharya, P. Sutter, A. Lorke, and M. Horn-von Hoegen

Phys. Rev. Lett. **108**, 266804 — Published 28 June 2012

DOI: [10.1103/PhysRevLett.108.266804](https://doi.org/10.1103/PhysRevLett.108.266804)

Manipulation of electronic transport in the Bi(111) surface state

G. Jnawali,^{1,*} C. Klein,¹ Th. Wagner,^{1,†} H. Hattab,¹ P. Zahl,² D. P. Acharya,^{2,‡} P. Sutter,² A. Lorke,¹ and M. Horn-von Hoegen¹

¹*Department of Physics and Center for Nanointegration Duisburg-Essen (CENIDE),
University of Duisburg-Essen, Lotharstr. 1, 47057 Duisburg, Germany*

²*Center for Functional Nanomaterials, Brookhaven National Laboratory, Upton, New York 11973, USA*

We demonstrate the controlled manipulation of the 2D-electronic transport in the surface state of Bi(111) through the deposition of small amounts of Bi to generate adatoms and 2D islands as additional scatterers. The corresponding increase in resistance is recorded in-situ and in real time. Model calculations based on mean field nucleation theory reveal a constant scattering efficiency of adatoms and of small 2D Bi islands, independent of their size. This finding is supported by a detailed scanning tunneling microscopy and -spectroscopy study at 5K which shows a highly anisotropic scattering pattern surrounding each surface protrusion.

PACS numbers: 73.25.+i, 68.49.Jk, 73.20.-r

Recently, thin bismuth (Bi) films have attracted much attention because of their remarkable surface electronic properties [1]. The Fermi surface of Bi(111) is composed of surface states which show strong spin-orbit splitting due to the broken inversion symmetry and strong spin-orbit coupling [2–7]. The sheet carrier density in this surface state, as deduced from the Fermi surface map or Hall measurements, is of the order of $n_{ss} \sim 0.5 - 1.5 \times 10^{13} \text{ cm}^{-2}$, which for film thicknesses below 10 nm is almost two orders of magnitude higher than the projected carrier density in the bulk ($\sim 10^{11} \text{ cm}^{-2}$) [4, 8, 9]. In recent works it has been confirmed that bulk conduction is negligible in ultrathin Bi films at low temperatures [9, 10].

One of the consequences of strong spin-split surface states in thin Bi films is the strong suppression of backscattering of electrons: the surface state is protected against scattering and perturbation. The spin-selective scattering rules impede the scattering probability between electronic surface states of opposite spin orientations [11–13] and will strongly reduce the influence of defects on the surface conductivity. However, despite the suppressed scattering, highly anisotropic quasi particle interferences, i.e., Friedel-type oscillation patterns, have been observed in the vicinity of point defects on the Bi(110) [11] and Bi(111) [14] surfaces. These findings indicate that backscattering may not be completely ruled out. The electron scattering contributions of individual surface defect states is therefore of fundamental interest for the understanding of the conductivity in this system and generally in protected material systems. While there has been substantial work exploring the electronic structure of such surface states by photoemission spectroscopy [15–17], very few direct electronic transport studies are available, which may shed light on the intriguing scattering mechanism.

In this letter, we show in an *in-situ* study how the 2D electron transport in the Bi(111) surface state can be manipulated by a well defined surface modification. Mor-

phological defects such as adatoms and small islands are introduced as electron scatterers through the deposition of sub-monolayer coverages of Bi on a smooth Bi(111) film at 80 K. The surface resistance and morphology can be determined during deposition which allows us to precisely correlate the electron scattering with surface defect density [10]. In contrast to a previous study, which employed oxidation of the Bi surface [8] our method constitutes a non-destructive and subtle manipulation of the surface state conductivity. It is even reversible since the original smooth surface can be recovered after annealing the film up to 450 K.

We find that the transport data can be modeled using mean-field theory to describe the formation of additional scattering centers on the surface during Bi deposition. Strikingly, our data show that the scattering efficiency is nearly identical for several types of surface scatterers, ranging from Bi adatoms to small 2D Bi islands. This is confirmed by low temperature scanning tunneling microscopy (LT-STM) measurements, which reveal an anisotropic scattering pattern with an amplitude that is independent of the surface topology, i.e., the size of the scatterers.

The surface transport measurements were performed under ultrahigh vacuum conditions at a base pressure of less than 2×10^{-10} mbar. A well-oriented *p*-type Si(001) wafer (miscut $< 0.2^\circ$) was cut into substrates with a size of $(3.5 \times 0.4 \times 0.05) \text{ cm}^3$ and prepared *in-situ* by degassing at 870 K for 6 hours and flash annealing at 1470 K for a few seconds by resistive heating. This process removes the native oxide and results in a (2×1) reconstruction at room temperature and $c(4 \times 2)$ at 80 K, indicating a clean surface with low-defect density [18].

Bi was deposited on the Si(001)- $c(4 \times 2)$ surface at 150 K by thermal evaporation from a ceramic crucible. During deposition, the pressure remained below 4×10^{-10} mbar. A deposition rate of 0.6 bilayers/minute ($1 \text{ BL} = 1.14 \times 10^{15} \text{ atoms/cm}^2$ with a Bi bilayer thickness of 0.394 nm) was maintained during each deposition

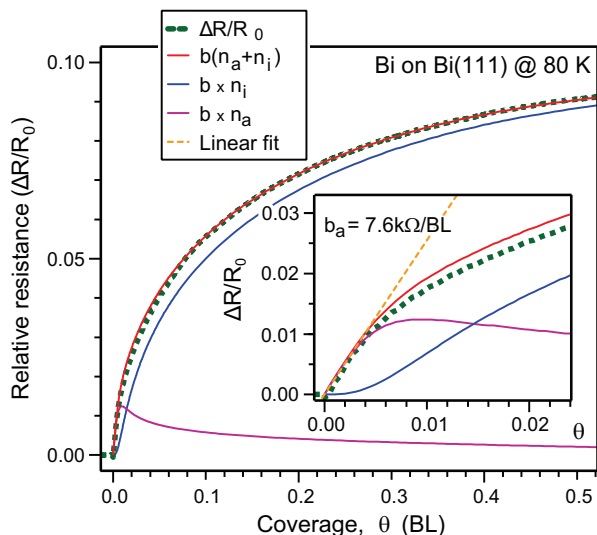


Figure 1: (a) Measured relative change of surface resistance (green dotted line) during deposition of Bi on a 9 nm Bi(111) base film at 80 K. The data are fitted with the total density of scatterers (adatoms n_a : purple line, islands n_i : blue line, total $(n_a + n_i)$: red line) and scaled by characteristic scattering efficiency b . The inset shows a closeup of the low-coverage regime with the dashed yellow line indicating the linear onset.

cycle. The deposition rate was monitored by a quartz crystal microbalance and was calibrated using low energy electron diffraction (LEED) intensity oscillations of the (00)-spot during layer-by-layer growth [19]. A 9 nm thick template Bi(111) film was prepared for the electrical transport measurements. Annealing of the Bi film and additional Bi deposition was followed according to the recipe published elsewhere [20]. This film shows high crystalline quality and atomically flat broad surface terraces (100 to 400 nm width) [21]. The integrity of the surface and the Bi film was confirmed by spot profile analyzing LEED during and after deposition [22, 23].

The electrical resistance was measured *in-situ* using tungsten disilicide (WSi_2) contacts in a four-point probe setup as described in detail elsewhere [24]. Ohmic contacts of WSi_2 are compatible with high-temperature surface preparation [24]. High-resistivity Si ($10^3 \Omega \text{ cm}$) was chosen to ensure carrier freeze-out at low temperatures. The initial flat Bi(111) film exhibits a resistance $R_0 = 7 \text{ k}\Omega$ at 80 K which corresponds to a sheet resistance of $\rho_0, 80\text{K} = 2300 \Omega/\square$, i.e., a sheet conductivity of $\sigma_0, 80\text{K} = 4.3 \times 10^{-4} \Omega^{-1}/\square$. These values are in good agreement with previous work [9]. The room temperature values $\rho_0, 300\text{K} = 760 \Omega/\square$ and $\sigma_0, 300\text{K} = 1.3 \times 10^{-3} \Omega^{-1}/\square$ agree with the results from Hirahara *et al.* [8]. This indicates dominant electronic transport through the surface states at 80 K, which is independent of film thickness [10].

To introduce scattering centers in a controlled fashion, additional Bi was deposited on the Bi film at 80 K,

leading to surface roughness in the form of adatoms and small 2D Bi islands [25]. The induced additional scattering manifests itself through a pronounced increase of the resistivity as shown in Fig. 1 where the normalized change in resistance $\Delta R/R_0 = [R(\theta) - R_0]/R_0$ is plotted with green dots as a function of the additional Bi coverage θ . As expected, at low coverage, where no islands have formed yet, the resistance increases linearly with the density of deposited Bi adatoms (see inset of Fig. 1). However, already at very low coverages of only 0.004 BL, $\Delta R/R_0$ becomes sublinear, indicating the formation of islands. After deposition of 0.5 BL an increase in the surface resistance between 9% and 17% is observed for different samples. This variation is attributed to subtle differences of the surface morphology in terms of either terrace size or step density distribution.

To model the influence of adatoms and nucleated islands on the surface-roughness-induced scattering, we start with a simple Drude-type resistivity ρ_{tot} and use Matthiessen's rule to separate the surface scattering from all other scattering processes [26]:

$$\rho_{tot} = \frac{m^*}{ne^2\tau_t} = \frac{m^*}{ne^2} \left(\frac{1}{\tau_0} + \frac{1}{\tau_s} \right) = \rho_0 + \rho_s. \quad (1)$$

Here, τ_t is the total mean scattering time, which consists of a background contribution (τ_0) and a contribution, that is caused by the deposition-induced surface roughness (τ_s). The effective mass is m^* , and n is the sheet density of the charge carriers. The resulting background and surface contributions ρ_0 and ρ_s to the resistivity are (apart from geometrical factors) equivalent to the background resistance R_0 and the surface-roughness-induced resistance R_s , respectively, so that we find for the total sheet resistance:

$$R_{tot} = R_0 + R_s. \quad (2)$$

Because we have measured the resistance *in-situ* at constant temperature (80 K), the background contribution R_0 will remain unchanged during the deposition process. Thus, the change in resistance $\Delta R = (R_{tot} - R_0) = R_s$, will directly reflect the surface scattering contribution due to adatoms and islands. Furthermore, for a given Fermi velocity v_F , the scattering time τ_s is inversely proportional to the scattering length ℓ_s and thus proportional to the density of scatterers n_s . Therefore, the resistance R_s will be directly given by the density of the surface scatterers: $R_s \propto 1/\tau_s = (v_F/\ell_s) \propto n_s$. Under our experimental conditions, adsorption of foreign adatoms can be neglected during deposition, i.e., the extra scattering is purely due to Bi adatoms and islands.

To estimate the number densities of adatoms n_a and islands n_i , we apply rate equations based on a mean-field nucleation theory [27, 28]. The rate equations for

the adatom and island densities are given by:

$$\frac{dn_a}{dt} = f - 2k_1n_a^2 - k_2n_an_i - f(ft - n_a) - 2fn_a \quad (3)$$

$$\frac{dn_i}{dt} = k_1n_a^2 + fn_a \quad (4)$$

where f is the deposition rate, k_1 , k_2 are the adatom-adatom and adatom-island capture rates, and t is the deposition time.

The five terms on the right-hand side of Eq. 3 denote (i) the increase of adatom density n_a due to evaporation with a constant flux f , and its decrease caused by (ii) collision of two adatoms, (iii) adatoms captured by existing islands, direct impingement of adatoms onto (iv) stable islands and onto (v) other adatoms. Equation 4 describes the increase in island density n_i due to adatom-adatom collision or caused by a direct hit of a deposited atom with an adatom as a consequence of term (v) from Eq. 3.

Equations 3 and 4 are simplified by assuming that both adatom-adatom and adatom-island capture rates are identical, i.e., $k_1 = k_2 = k$, as supported by growth studies in metallic systems [29, 30]. For simplicity, we normalize the units for the deposition rate and coverage, i.e., $f = 1$ and the coverage $\theta = ft = t$. Equations 3 and 4 are solved numerically to obtain adatom and island densities. The calculated island density n_i exhibits a cubic-root behavior with coverage in agreement with a previous study on sub monolayer Bi growth [25].

As discussed above, the change in resistance is proportional to the density of scatterers:

$$\frac{\Delta R}{R_0} = \frac{R_s}{R_0} = b_a n_a(\theta) + b_i(\theta) n_i(\theta). \quad (5)$$

Here, the coefficients b_a and $b_i(\theta)$ correspond to the scattering efficiency of adatoms and islands, respectively. The adatom scattering efficiency $b_a = 7.6 \text{ k}\Omega/\text{BL}$ can be determined by the linear slope of the resistance change at the onset of evaporation ($\theta \rightarrow 0$). The scattering efficiency of the islands $b_i(\theta)$ and its dependence on coverage can only be determined by fitting the complete data set. We have investigated different models for $b_i(\theta)$, including a linear dependence on either the average island area or the perimeter. As it turns out, the calculated data is quite sensitive to variations of the model parameters because of the pronounced peak of the adatom density $n_a(\theta)$ (see Fig. 1), which is perfectly offset by the increase in $n_i(\theta)$, resulting in a smooth, featureless curve for ΔR . Surprisingly, we find the best fit for $b_i(\theta) = b_a = \text{const.} \equiv b$, i.e., the scattering efficiency of a small 2D island is constant and equal to the cross-section of an adatom. Figure 1 shows the calculated contributions $b \cdot n_a$ (purple line) and $b \cdot n_i$ (blue line), to the total change in resistance ΔR (red line), as well as the experimental results (green dots). The good agreement over the entire range of data gives us confidence that the

approach and the assumptions for calculating ΔR are justified – in particular $k_1 = k_2 = k$ and $b_i(\theta) = b_a = b$.

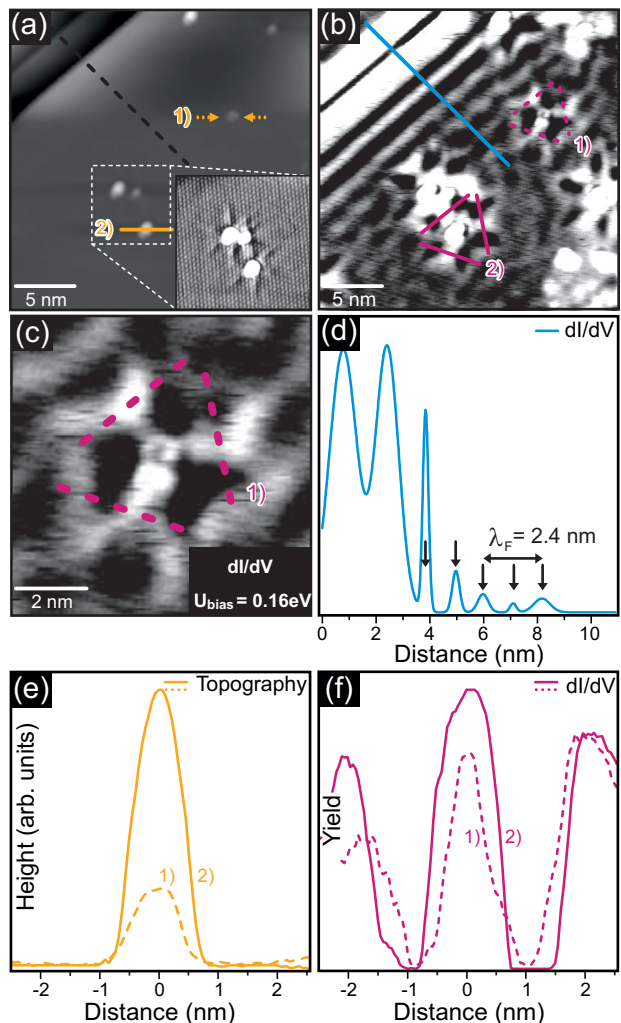


Figure 2: (a) Constant current STM image of a Bi(111) surface (tunneling parameters: $U_{\text{bias}} = -0.16 \text{ V}$, $I = 0.5 \text{ nA}$, field of view 25 nm) shows atomically resolved Bi(111) terraces separated by bilayer steps. The inset shows weak star-like height corrugations surrounding each adatom or 2D-island. (b) A dI/dV map ($U_{\text{bias}} = 0.16 \text{ V}$) of the same region. A distinct standing wave pattern caused by interference of scattered electrons at a step edge is visible. Each adatom and island shows an anisotropic threefold symmetric scattering pattern. Bright areas correspond to higher topography and larger LDOS, respectively. (c) Closeup of the anisotropic scattering pattern of the point-like structure shown in (b). (d) Profiles of the dI/dV map taken across the step edge. From the periodicity of the standing wave pattern, a Fermi-wavelength of 2.4 nm is estimated. (e) STM apparent height profiles measured across two different scattering centers (small protrusions) marked in the topographic image, (a). (f) Profiles across the scattering patterns in the dI/dV map, (b), averaged from the three profiles indicated by purple lines (solid and dotted).

To further support these striking findings and to better

understand the scattering field surrounding adatoms and islands, we performed both, STM and tunneling spectroscopy measurements at 5 K on an identically prepared Bi film with an additional coverage of 1/1000 BL. Figure 2(a) depicts a topographic image of such a prepared sample. It shows one flat terrace, two bilayer high steps (upper left corner), and small protrusions that we attribute to the additional Bi deposition at 5 K. As already shown in Fig. 2(a) and quantified in (e) the adatoms and 2D islands differ greatly in size. Furthermore, with enhanced contrast, the topographic image reveals a star-like scattering pattern surrounding each protrusion, as shown in the inset of Fig. 2(a). We attribute this to Friedel-type oscillations of the local density of states and therefore recorded the corresponding dI/dV map. Fig. 2(b) shows in the dI/dV map a threefold symmetric pattern surrounding each scatterer. Such an anisotropic pattern is caused by spin-allowed scattering processes and the superposition of scattered plain waves in a surface state with a highly anisotropic Fermi surface [14]. Interestingly, while the topology of the scatterers differs considerably, the amplitude and the lateral extent of the scattering pattern are quite similar. To better quantify this observation we have taken three line profiles surrounding the protrusion marked by 1) and 2). The averaged dI/dV profiles are plotted in Fig. 2(f). While the topographic size (e) of these two scatterers differs by more than a factor of 3, the amplitude of the scattering pattern (f) is almost the same. These findings confirm our conclusion that adatoms and islands exhibit the same scattering efficiency, i.e., $b_a = b_i$.

The pronounced standing wave pattern originating from the step edge as seen in Fig. 2(b) and plotted in (d) allows us to determine the typical wavelength at the Fermi energy to be $\lambda_F = 2.4$ nm. This is considerably larger than the island size D obtained from experimental data [19, 25]. It also exceeds by far the island size obtained from our calculations, which increases from 2 to 13 atoms in the range shown in Fig. 1. From the adatom scattering efficiency b_a (change in resistance per additional adatom), the 2D electron density n_{ss} , and the Fermi wavevector k_F , it is possible to estimate the scattering cross section of a single adatom $\Sigma = b_a n_{ss} e^2 / (\hbar k_F) \sim 4 \cdot 10^{-12}$ m. This very small value indicates that even though the electrons are located in a surface state, they are very little affected by the intentionally introduced surface scattering centers.

In conclusion, we have demonstrated that even in complex systems such as Bi(111), which exhibit a strongly anisotropic electronic scattering pattern, the low temperature conductivity can be well explained using a simple Drude-type approach. Surprisingly, however, at least for scatterers that are smaller than the typical wavelength at the Fermi energy, the scattering cross section is independent of the size of the scatterers and much smaller than their physical dimension. The impact of our finding

could go far beyond the study of Bi surfaces, because this system can be considered a model system for transport studies in protected surface states.

Financial support from the Deutsche Forschungsgemeinschaft through SFB 616 “Energy Dissipation at Surfaces” is gratefully acknowledged. Research carried out in part at the Center for Functional Nanomaterials, Brookhaven National Laboratory, which is supported by the U.S. Department of Energy, Office of Basic Energy Sciences, under Contract No. DE-AC02-98CH10886.

* Electronic address: gr.jnawali@uni-due.de; present address: Department of Physics and Electrical Engineering, Columbia University, New York, NY 10027.

† Present address: Johannes Kepler University Linz, Institute of Experimental Physics, Altenberger Str. 69, A-4040 Linz, Austria.

‡ Present address: Pacific Northwest National Laboratory, Richland, Washington 99352, USA

- [1] Ph. Hofmann, Prog. Surf. Sci. **81**, 191 (2006).
- [2] É. I. Rashba, Sov. Phys. Solid State **2**, 1109 (1960).
- [3] L. Petersen, P. Hedegård, Surf. Sci. **459**, 49 (2000).
- [4] C. R. Ast and H. Höchst, Phys. Rev. Lett. **87**, 177602 (2001).
- [5] Yu. M. Koroteev, G. Bihlmayer, J. E. Gayone, E.V. Chulkov, S. Blügel, P. M. Echenique, and Ph. Hofmann, Phys. Rev. Lett. **93**, 046403 (2004).
- [6] T. Hirahara, T. Nagao, I. Matsuda, G. Bihlmayer, E. V. Chulkov, Yu. M. Koroteev, P. M. Echenique, M. Saito, and S. Hasegawa, Phys. Rev. Lett. **97**, 146803 (2006).
- [7] T. Hirahara, K. Miyamoto, I. Matsuda, T. Kadono, A. Kimura, T. Nagao, G. Bihlmayer, E. V. Chulkov, S. Qiao, K. Shimada, H. Namatame, M. Taniguchi, and S. Hasegawa, Phys. Rev. B **76**, 153305 (2007).
- [8] T. Hirahara, I. Matsuda, S. Yamazaki, N. Miyata, S. Hasegawa, and T. Nagao, Appl. Phys. Lett. **91**, 202106 (2007).
- [9] D. Lükermann, S. Sologub, H. Pfñür, and C. Tegenkamp, Phys. Rev. B **83**, 245425 (2011).
- [10] G. Jnawali, Th. Wagner, H. Hattab, R. Möller, A. Lorke and M. Horn-von Hoegen, e-J. Surf. Sci. Nanotech. **8**, 27 (2010).
- [11] J. I. Pascual, G. Bihlmayer, Yu. M. Koroteev, H.-P. Rust, G. Ceballos, M. Hansmann, K. Horn, E. V. Chulkov, S. Blügel, P. M. Echenique, and Ph. Hofmann, Phys. Rev. Lett. **93**, 196802 (2004).
- [12] P. Roushan, J. Seo, C. V. Parker, Y. S. Hor, D. Hsieh, D. Qian, A. Richardella, M. Z. Hasan, R. J. Cava and A. Yazdani, Nature **460**, 1106 (2009).
- [13] J. Seo, P. Roushan, H. Beidenkopf, Y. S. Hor, R. J. Cava, and A. Yazdani, Nature **466**, 343 (2010).
- [14] M. C. Cottin, C. A. Bobisch, J. Schaffert, G. Jnawali, A. Sonntag, G. Bihlmayer, and R. Möller, Appl. Phys. Lett. **98**, 022108 (2011).
- [15] Y. L. Chen et al., Science **329**, 659 (2010).
- [16] D. Hsieh and D. Qian and L. Wray and Y. Xia and Y. S. Hor and R. J. Cava and M. Z. Hasan, Nature **452**, 970 (2008).
- [17] S.-Y. Xu et al., Science **332**, 560 (2011).

- [18] R. A. Wolkow, Phys. Rev. Lett. **68**, 2636 (1992).
- [19] G. Jnawali, H. Hattab, C. A. Bobisch, A. Bernhart, E. Zubkov, R. R. Möller, and M. Horn-von Hoegen, Phys. Rev. B **78**, 035321 (2008).
- [20] G. Jnawali, H. Hattab, B. Krenzer, and M. Horn-von Hoegen, Phys. Rev. B **74**, 195340 (2006).
- [21] H. Hattab and E. Zubkov and A. Bernhart and G. Jnawali and C. Bobisch and B. Krenzer and M. Acet and R. Möller and M. Horn-von Hoegen, Thin Solid Films **516**, 8227 (2008).
- [22] U. Scheithauer, G. Meyer, and M. Henzler, Surf. Sci. **178**, 441 (1986).
- [23] M. Horn-von Hoegen, Z. Kristallogr. **214**, 591 & 684 (1999).
- [24] G. Jnawali, F.-J. Meyer zu Heringdorf, D. Wall, S. Sindermann, and M. Horn-von Hoegen, J. Vac. Sci. Technol. B **27**, 180 (2009).
- [25] G. Jnawali, Th. Wagner, H. Hattab, R. R. Möller, and M. Horn-von Hoegen, Phys. Rev. B **79**, 193306 (2009).
- [26] C. Kittel, *Introduction to Solid State Physics* (Wiley, 2005).
- [27] J. A. Venables, G. D. T. Spiller, and M. Hanbücken, Rep. Prog. Phys. **47**, 399 (1984).
- [28] H. Brune, Surf. Sci. Rep. **31**, 121 (1998).
- [29] M. J. Stowell, Phil. Mag. **26** (2), 361 (1972).
- [30] J. A. Venables, Phil. Mag. **27** (3), 697 (1973).